Heterogeneous sorption of radionuclides predicted by crystal surface nanoroughness

Yuan, T.; Schymura, S.; Bollermann, T.; Molodtsov, K.; Chekhonin, P.; Schmidt, M.; Stumpf, T.; Fischer, C.;

Originally published:

November 2021

Environmental Science & Technology 55(2021)23, 15797-15809

DOI: https://doi.org/10.1021/acs.est.1c04413

Heterogeneous sorption of radionuclides predicted by crystal surface nanoroughness

Tao Yuan*[1], Stefan Schymura[1], Till Bollermann[1], Konrad Molodtsov[1], Paul Chekhonin[1], Moritz Schmidt[1], Thorsten Stumpf[1], and Cornelius Fischer[1]

[1]Institute of Resource Ecology, Helmholtz-Zentrum Dresden-Rossendorf (HZDR), Dresden, Saxony, 01328, Germany

*Corresponding Author: t.yuan@hzdr.de

ABSTRACT

Reactive transport modeling (RTM) is an essential tool for the prediction of contaminants' behavior in the bio- and geosphere. However, RTM of sorption reactions is constrained by the surface site assessment. The reactive site density variability of the crystal surface nanotopography provides an "energetic landscape", responsible for heterogeneous sorption efficiency, not covered in current RTM approaches. Here, we study the spatially heterogeneous sorption behavior of Eu(III), as an analogue to trivalent actinides, on a polycrystalline nanorough calcite surface and quantify the sorption efficiency as a function of surface nanoroughness. Based on experimental data from micro-focus time-resolved laser-induced luminescence spectroscopy (μTRLFS), vertical scanning interferometry (VSI), and electron back-scattering diffraction (EBSD), we parameterize a surface complexation model (SCM) using surface nanotopography data. The validation of the quantitatively predicted spatial sorption heterogeneity suggests that retention reactions can be considerably influenced by nanotopographic surface features. Our study presents a way to implement heterogeneous surface reactivity into a predictive SCM for enhanced prediction of radionuclide retention.

Keywords: Sorption reactions, Crystal surface reactivity, μTRLFS, Surface complexation modeling, Radionuclide migration

INTRODUCTION

The potential migration of actinides constrains the safety assessment of disposal concepts for nuclear waste in deep geological formations. Such concepts for underground storage facilities require reliable predictions for 100,000s of years to diagnose potential migration of stored radionuclides into the biosphere. Reactive transport models are crucial in providing such predictions and the heterogeneity of physicochemical input values defines the reliability of the numerical results. A key challenge is the upscaling of the molecular processes to quantify the radionuclide retention processes, bridging the gap from laboratory scale experiments to large scale facilities. Molecular mechanistic insights are provided experimentally and analytically by spectroscopic techniques such as Time-Resolved Laser Fluorescence Spectroscopy (TRLFS)[1, 2], and Extended X-ray Absorption Fine Structure Spectroscopy (EXAFS)[3, 4], and numerically by molecular dynamic simulations (MD), providing insights into the structure of the adsorbed ions at specific surface sites[5, 6]. Upscaling and implementing these insights into continuum scale reactive-transport models is challenging because of the intrinsic variability of surface reactivity at the pore scale. Typical RTM approaches employ uniform surface parameters such as specific surface area (SSA) and site density, uniform electrostatic diffuse layer potentials, and simplified uniform surface protonation models to simulate adsorption processes of radionuclides through various surface complexation reactions implemented by surface complexation models (SCM)[7-13] to yield a simple retention coefficient in RTM at the continuum scale[14-16]. Consequently, simplifications such as the assumption of macroscopically homogeneous behavior[17] as well as surface area normalizations[18] are commonly applied. These simplifications limit our ability to model and predict the consequences of varying surface reactivity.

Analytically, the recent development of the µTRLFS technique allows us to identify interfacial speciation with µm-spatial resolution and the very high sensitivity required to investigate surface

complexes[19, 20]. This technique revealed heterogeneous sorption behavior of the trivalent actinide analog Eu(III) on a granite rock surface that cannot be quantitatively explained by mineral type and composition alone[19]. Consequently, insight into the intrinsic variability of surface reactivity is required to improve our predictive capabilities of reactive transport processes[21]. The surface reactivity may depend on several factors, including crystal defects and surface nanotopography as well as crystal orientation. From an energetic point of view, a dominant factor is the kink site density (KSD) of the crystal surface.[22] Figure 1 illustrates different nanotopographic configurations of the crystal surface with specific kink site densities. With increasing KSD, these include (1) atomically flat terraces with point defects, (2) etch pits walls with steps and kinks resulting from dissolution processes, (3) surface steps with kinks along cleavage planes, and (4) very rough surface portions with a multitude of edge and kink sites owing to mechanical treatment (polishing, grinding, preparation of powdered sample material) of crystalline matter. Previous studies suggested that increasing KSD results in enhanced surface reactivity for, e.g., sorption[23].

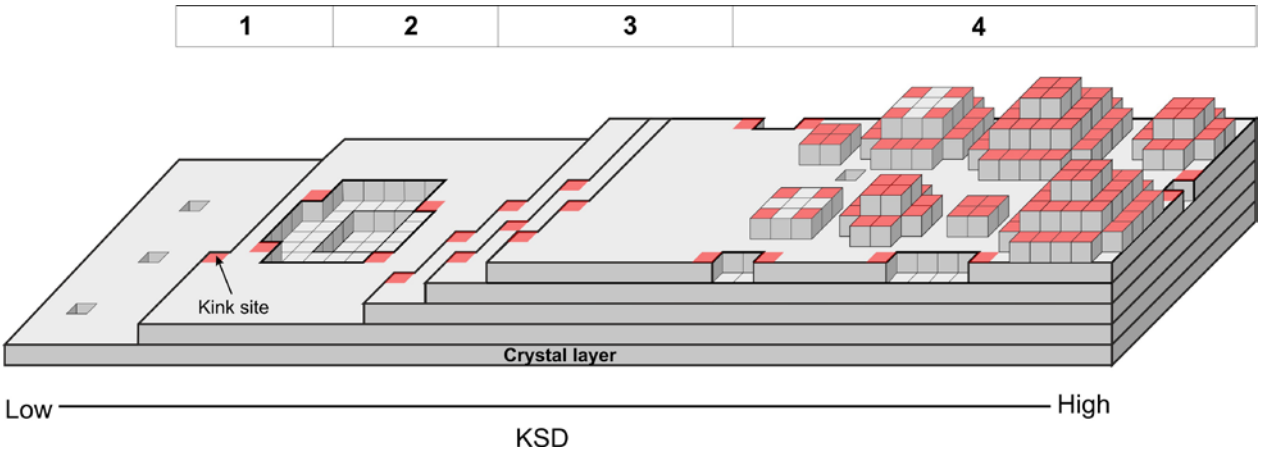

Figure 1 Schematic representation of nanotopographic characteristics of a crystal surface, showing (1) an atomically flat terrace with point defects, (2) an etch pit wall with steps and kinks, (3) surface steps with kinks due to crystal cleavage, and (4) a very rough surface due to mechanical treatment such as polishing. Kink sites are marked in the red color and the kink site density increases from left to right in this scheme.

Here, we investigate the sorption of Eu(III) on calcite to experimentally exemplify the variability of surface reactivity as a function of surface nanotopography of monomineralic but polycrystalline collector surfaces during sorption processes. Eu(III) serves as a luminescent probe with excellent spectroscopic properties[24] and a chemical analogue for the trivalent actinides, some of which (Am(III), Pu(III)) determine the radiotoxicity of nuclear wastes over 100,000s of years. Calcite was selected as one of the most widely distributed mineral phases in the earth's crust, with demonstrated importance for the migration of radionuclides[25] and other contaminants in the geosphere[26], by both, the complexation reactions at the mineral surface[27, 28] as well as incorporation processes within the crystal lattice.[25, 29] Due to the presence of only a single mineral phase in this study, we can exclude mineralogical effects and instead focus on the surface energy variability induced by crystallography or topography. Our strategy is the quantitative mapping of surface sorption efficiency data, including information about speciation and hydration of Eu(III) using µTRLFS[19]. These data are correlated with surface nanotopography maps from vertical scanning interferometry and crystal orientation data from electron backscatter diffraction (EBSD) analysis. The spatially-resolved information allows us to parameterize an improved SCM using surface nanoroughness data that account for heterogeneities in crystal surface energy, and which makes it possible to predict heterogeneous sorption behavior. The modeling results were validated using experimental data from µTRLFS.

METHODS

Experimental setup. Two calcite samples were utilized to investigate the effect of the different nanotopographical endmembers on the sorption efficiency of Eu(III) on the crystal surface. One sample was a polished calcite crystal with a high density of edge and kink sites due to the its rough surfaces (manufacturer: KORTH Kristalle GmbH, Altenholz, polished along (10-14), the other is a cleaved calcite surface (calcite island spar, Chihuahua, Mexico, WARD's 46E1438) with varying

degrees of step densities analyzed by VSI. The two samples were exposed to 10^{-6} M aqueous $[^{152}Eu]Eu(NO_3)_3$ in 0.1 M NaCl solution at pH 7.5 by immersing their surface upside down in the solution for 15 minutes. No alterations of the surface topography are detected using interferometry microscopy surface analysis. The sorption was quantified via autoradiographic imaging using a BAS-IP SR storage phosphor screen that was read out with a pixel size of 25 µm after exposure using an Amersham Typhoon Biomolecular Imager (GE Lifesciences). Absolute concentrations were yielded by calibration of the image in ImageJ using a series of europium standards of known concentration.

As a second step, the investigations were then expanded to a more realistic system with respect to calcite-bearing host rocks. Another sorption experiment was performed using polycrystalline calcite. A cylindrical drilled marble sample (diameter: 1.5 cm, length: 1 cm, Großsoelk, Austria, composition: calcite (95 wt. %), quartz (< 2 wt. %), muscovite (< 1 wt. %), phlogopite (< 1 wt. %) and ore minerals (<1 wt. %)[30], was polished using an oil-based mono-crystalline diamond suspension (crystal size: 50 nm) and partially masked with a layer of 550 nm of gold[31] as a height reference for surface analysis at the nanometer scale. To identify the crystallographic orientation of the crystal grains in the sample surface a grid of 200 x 150 points (resolution: 10 µm) was analyzed with EBSD using a Zeiss NVision 40 scanning electron microscope equipped with a Bruker e$^-$Flash^{Hr}- detector and a QUANTAX CrystAlign EBSD-System (acceleration voltages: 10kV, beam current: 2.5nA).[32] First, to provide a surface roughness variability similar to what is expected in natural systems after diagenetic reactions, a dissolution experiment was performed by reacting the sample surface with air-equilibrated, aqueous 2.2 mM Na_2CO_3 at pH 8.8 for 1 hour using a custom-made flow-through cell (cell volume: 300 µL, flowrate: 30 mL/h). The experimental conditions are identical to those described in the literature for studying dissolution kinetics of calcite surfaces at far-from-equilibrium conditions[22]. Second, a batch europium sorption

experiment was conducted by immersing the sample surface into a solution of 10^{-5} mol/L $Eu(NO_3)_3$ and 0.1 mol/L NaCl with a pH value of 8.5 for 24 hours. In this step, the larger concentration and longer sorption period were made necessary to enable the µTRLFS studies[19, 20]. The sample was then rinsed with the background solution and dried. Spatially resolved information on the europium sorption efficiency and the adsorbed species was gained using µTRLFS mapping of a 0.5 mm × 1.5 mm subsection with a spatial resolution of 20 µm.

The surface topographies of all the samples were analyzed using a Sensofar S neox white-light vertical scanning interferometer equipped with Nikon DI interferometry objectives for 20 ×, 50 ×, and 100 × magnifications (see SI, Table S1 for detailed specifications).

µTRLFS. µTRLFS measurements were conducted with a setup designed in-house as described in Molodtsov et al. 2019[19]. The laser beam was provided by a pumped (Surelite SL I-20 @ 355 nm, Continuum) dye laser (NarrowScan @ Exalite 389/398 1:1 mix, Radiant Dyes). The pulse energy was set to approximately 20 µJ to prevent possible laser ablation. The wavelength was fixed at 394 nm to maximize the light absorption of Eu^{3+} ($^7F_0 \rightarrow {}^5L_6$ transition) resulting in higher sensitivity for luminescence detection[24]. The laser beam was focused by a 50x long-distance objective (MLWD-50X, Newport) to a spot with approximately 20 µm in diameter. The sample surface was aligned to the focal plane of the laser beam with a z-stage (KT-RS60, Zaber) and then scanned in a 20 µm grid with an x-/y-stage (M-423 driven by TRB25CC and controlled with CONEX-CC, Newport). The gathered luminescence light was redirected to the detector (Shamrock SR303i spectrograph combined with DH320T-18U-63 iCCD camera, Andor) to collect the full spectral information in each data point. Spectra were measured with 100 accumulations over 5 seconds in total with a gate width and exposure time of the iCCD of 10 ms. To evaluate the data a python-based software (pycroTRLFS EVAL, HZDR) was used. The spectra were analyzed with respect to the peak areas of the $^5D_0 \rightarrow {}^7F_1$ ($^7F_1$) and $^5D_0 \rightarrow {}^7F_2$ ($^7F_2$) transitions and their fluorescence decays

after applying a linear background correction. The fluorescence intensity (sum of peaks $^7F_1$+ $^7F_2$) is correlated to the number of Eu(III) atoms and therefore corresponds to the sorption efficiency. The sorption efficiency of each pixel was calculated by normalizing the peak sum by the highest measured luminescence signal. The luminescence peak ratio (F_2/ F_1) corresponds to the sorption strength and also serves as a distinguishing indicator for speciation because the F_2 peak is a hypersensitive electric multipole transition, and its intensity reacts strongly to changes in Eu(III)'s chemical surroundings, while the F_1 peak as a magnetic dipole transition is mainly unaffected.[24] Lifetimes of the luminescence decays were recorded in several selected data points. The luminescence decay patterns could be reconstructed by bi-exponential decay functions with a fixed long lifetime of 3600 µs, which represents the well-known lifetime of the Eu^{3+} incorporation species into the crystal lattice of calcite.[25] This fixation is useful because the long-lived species usually have a quite low luminescence intensity, which is therefore much more affected by background correction uncertainties. As a result, the short lifetime can then be determined much more reliably. In some cases, the observed luminescence decay pattern was described by a mono-exponential decay function for residual-minimization purposes. The resulting lifetimes were then correlated to the number of remaining water molecules $n(H_2O)$ in the first coordination sphere of Eu^{3+} by the empirical equation[33, 34]:

$$n(H_2O) \pm 0.5 = \frac{1.07}{\tau} - 0.62, \quad (1)$$

where τ denotes the measured luminescence lifetime (in a unit of ms). The value of n can range from zero (incorporation) up to nine remaining water molecules (fully hydrated Eu^{3+} aquo ion). Intermediate amounts of water molecules left correspond to inner sphere complexation of the Eu^{3+} ion, here sorption to the calcite surface.

Sorption data analysis. Areas of different quantities of sorption were identified in the autoradiogram of the polished and cleaved samples and representative high-resolution topography

images were recorded. The sorption data on the polycrystalline calcite material from µTRLFS with a pixel size of 20 µm were cross-referenced with different grains (A-J) identified by EBSD. The grains were ordered with increasing europium sorption (see Figure S1) and Student t-tests were performed to analyze statistically significant differences in europium sorption (p=0.05). The data from neighboring grains with no statistically significant differences were combined into single datasets. This created four combined datasets with statistically significant differences in europium sorption efficiency, AF, IJHG, EDC, and B (in order of increasing europium sorption, see Table S2 and S3). Of the four datasets the grains with the most available data points – A, I, D, and B (in order of increasing europium sorption) – were chosen for a more detailed correlative analysis of the europium sorption and surface nanoroughness. VSI maps of each grain were measured and Sq values, the root mean square deviation or the standard deviation of the height data, of 20 µm × 20 µm pixels were extracted from the images and correlated with the µTRLFS sorption data.

For a more detailed investigation, the 20 µm × 20 µm pixels were each divided into subpixels with a smaller field of view (FOV) down to a maximum of 64 subpixels with a minimum FOV of 2.5 × 2.5 μm^2 which were analyzed according to their Sq value. The applied minimum FOV size of topographic data utilized for the calculation of the Sq parameter is limited by the spatial resolution and consecutive bisection algorithm used. The resulting datasets of Sq values were then averaged for every original pixel to mitigate the influence of larger structures such as scratches and holes in the crystal surface on the Sq-data (note that averaging the Sq values of the subpixels and measuring one Sq value for the whole pixel will give different results, with a higher influence of extreme values with the latter approach). These converged datasets were then correlated with the europium sorption efficiency. In a separate analysis different Sq ranges were investigated for their correlation with the sorption efficiency by only averaging the subpixels with Sq values in the ranges of 0-5 nm, 5-10 nm, 10-50 nm, and >50 nm (see Figure S2).

Numerical model. According to the lifetime analysis, we utilized the surface complexation reactions to describe Eu^{3+} adsorption on the calcite surface in a short time experiment. Therefore, the SCM was developed using the aqueous speciation reactions and surface complexation reactions in Table S4. The SCM is an electrostatic double-layer model [11, 13] in which the net surface charge balances the net charge in the diffuse layer[7]. The identical site density and specific surface area (SSA) are 5 sites/nm^2 and 0.262 m^2/g, respectively[28]. The chemical reactions were calculated using PHREEQC v3.5[7] with the Nagra/PSI Chemical Thermodynamic Database[35]. The SCM results were validated using measured sorption efficiency data from Zavarin et al. 2005[28] (Figure S3 in SI).

Parametrization of the predictive model. The topographical data for the predictive model is obtained from phase shifting interferometry (PSI) measurement with a high spatial resolution of 46 nm × 46 nm. The Sq value of each pixel is calculated at a 0.46 × 0.46 μm^2 FOV using 10 × 10 pixels of the surface topography data. Since the averaged Sq value is sensitive to the FOV, the calibration curve for the predictive modeling was adapted for the higher resolution. Based on the experimentally validated correlation of the optimized slope α with the FOV of the Sq value for ROI I and II (Figure S4 in SI), α was set to 0.03 for the predictive modeling. See below for a detailed discussion of these procedures. The use of a slope not specifically optimized for the surface in question may cause deviations in the prediction of the sorption efficiency, however, the predicted spatial sorption patterns and their trends with the evolution of the surface are valid.

RESULTS AND DISCUSSION

Calcite nanotopography effects on Eu(III) sorption. The influence of surface topography on sorption efficiency was studied using calcite crystal samples with different topographies that allowed us to isolate the effects of specific surface features. The use of single-crystal samples allowed us to study specific structural endmembers, i.e. very low KSD to very high KSD, even though the exact KSDs are not accessible to measurement. Figure 2 shows the surface topographies

of a cleaved and a polished calcite crystal (I) and the absolute concentrations of sorbed Eu(III) in a cleaved edge area (A), a cleaved terrace (B), and a fine-polished surface (C) (II). The polished crystal surface (C, Figure 2I) exhibits a highly nanorough surface that consists of a high amount of kink sites due to the fine polishing (cf. Figure 1 surface 4) producing a surface that may be linked to a powder sample. On the surface of the cleaved sample, two distinct structural features can be observed: distinct steps (A) that contain various degrees of steps according to the height difference (cf. Figure 1 surface 3) and flat terraces (B) in between the steps that can are made up by the large flat areas with a low amount of step density and point defects (cf. Figure 1 surface 1). Figure 2II shows the different concentrations of sorbed europium that the surface features A, B, and C lead to, as quantified by autoradiography. The highest amount of sorbed Eu(III) can be observed on the polished sample with a highly nanorough surface while the cleaved terrace with an approximately flat surface exhibits the lowest one, with the edge structure falling in between.

The observed heterogeneous sorption behavior suggests a variability of surface reactivity that reflects a heterogeneous distribution of crystal surface energy that can be quantified by surface topography analysis. The surface energy strongly depends on the number of surface building blocks such as kink sites and step edges[17]. A previous study[22] investigated heterogeneous surface reactivity and the probability of variations in kink site density. Additional literature data[36, 37] confirm the importance of the surface kink sites as the dominating intrinsic factor of enhanced surface reactivity during, e.g., dissolution and precipitation reactions. We thus hypothesize that such surface energy distribution affects the sorption efficiency, as suggested by kinetic Monte Carlo simulations (KMC) at the atomic scale[38]. Moreover, a molecular dynamics (MD) study investigating the reactivity of the calcite-water interface shows the number of surface reactive sites for adsorbing water molecules is higher at rough surface positions with kink sites and step edges compared to the flat surface portions with no surface roughness[5].

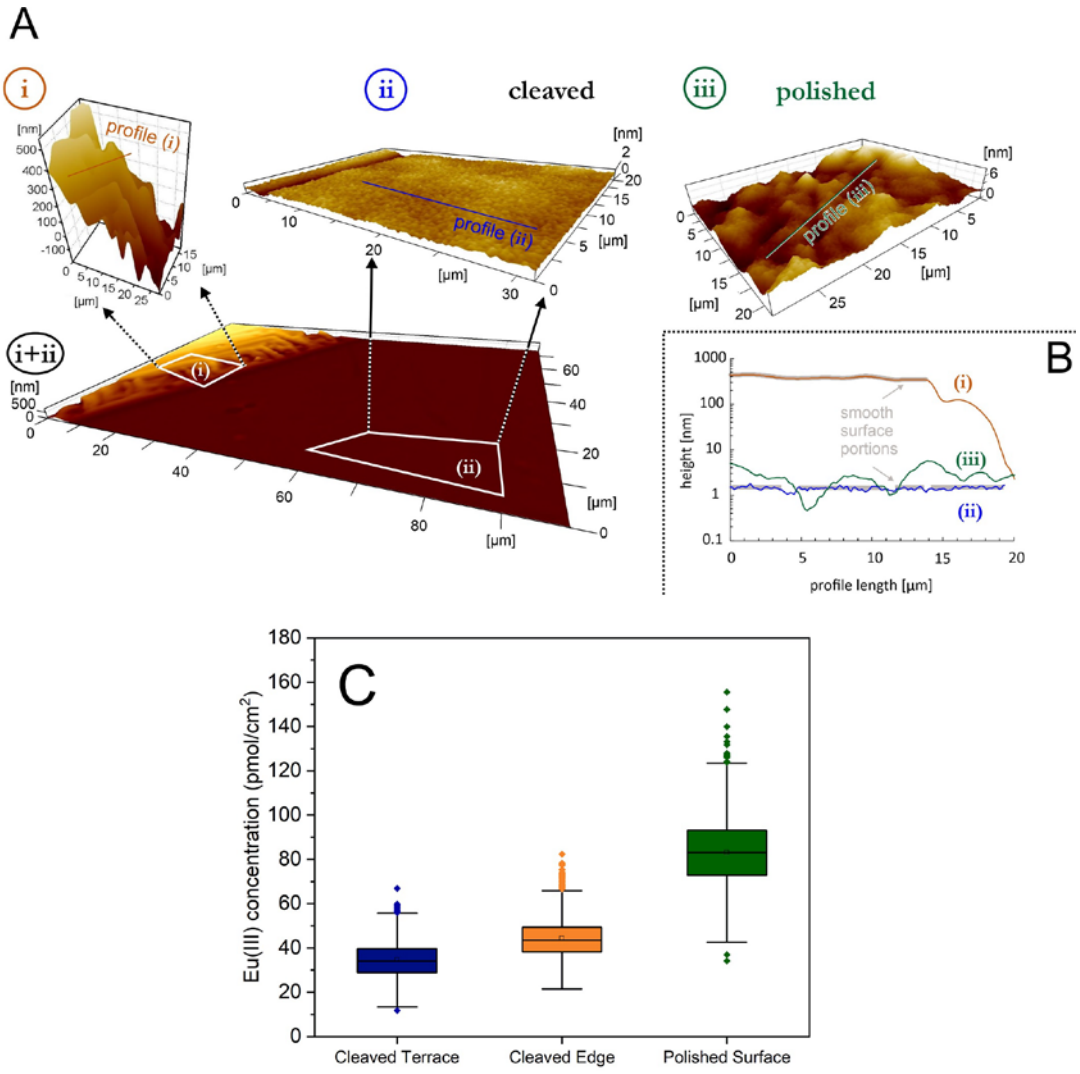

Figure 2. (A) surface topographies of cleaved calcite surface ((i) and (ii)) and polished calcite surface (iii). (i) shows a stepped edge due to cleaving with an overall height of about 500 nm. (ii) shows a flat cleavage plane with a maximum height of ~2 nm due to a single scratch along the otherwise flat surface. Note the different exaggerations of the z scale compared to the x and y scale of the maps (i-iii). **(B)** shows height distributions of the profile lines (i), (ii), and (iii). **(C)** Box-Whisker plots of the measured absolute concentrations of sorbed Eu(III) among the areas (i), (ii), and (iii). The quantitative concentration trend indicates the effect of crystal surface nanotopography (cf. Fig. 1) on sorption efficiency.

Heterogeneous sorption of Eu(III) on polycrystalline calcite. Now, we investigate the surface of polycrystalline calcite towards variability in sorption efficiency. Figure 3 shows an overview of the investigated calcite crystal surface maps including (a) the surface topography, (b) crystal orientations of the polycrystalline calcite material, (c) normalized sorption efficiency including selected spots where fluorescence lifetimes were collected, and (d) speciation distribution. The surface is composed of multiple crystal grains with diameters of about 10 µm to several 100 µm with varying crystal orientation. The sorption efficiency was determined based on the total luminescence intensity of Eu(III) as described in the methods section. The luminescence intensity reveals a heterogeneous distribution of the Eu(III) sorption, even within single crystal faces, varying by a factor of around 10 between lowest and highest concentrations. Several grains show statistically significant differences in sorption efficiency, however, no correlation between crystal orientation and sorption efficiency is found (see below and SI). An analysis of the ratio of the $^5D_0 \rightarrow {}^7F_2$ and $^7F_1$ luminescence transitions and lifetimes of the excited states provides information on the speciation of Eu(III) on the sample surface, as they are influenced by the bond strength[24] and the number of water molecules[33] in the first coordination sphere of the excited europium (see SI for detailed analysis of luminescence lifetime and speciation). In contrast to the heterogeneously distributed sorption efficiency, the mapping of the $^7F_2/\ ^7F_1$ peak ratio which is correlated to speciation (Figure 3d) shows a mostly homogeneous distribution. Most pixels exhibit peak ratios ~5, indicating that the dominant speciation of Eu(III) is surface sorption or incorporation species. A few pixels show a peak ratio of seven or above, but only where the luminescence intensity is very low, which leads to larger uncertainties in the determination of the peak ratios.

The measured lifetimes at selected surface sites (see Figure 3c, circles) are shown in the SI (Table S5). We generally find two distinct lifetimes: A short lifetime, which correlates to ~2 H_2O in the coordination sphere of Eu(III) and a longer lifetime which indicates a complete loss of hydration.

The short lifetime in combination with the typical peak ratio discussed above can be interpreted as an inner-sphere surface sorption complex that has been previously reported[25, 39]. This species is only present where the luminescence intensity is high and can be considered to be the major fraction of Eu on the mineral surface. The long lifetime and thus complete loss of hydration suggest incorporation into the calcite lattice[25]. The species appears homogeneously distributed over the whole surface, albeit always only in low quantities. As Eu is a common impurity in natural calcites[40], and because it seems unlikely that incorporation occurred in the short duration of our experiments[29] we interpret this species as Eu(III) incorporated into the natural calcite before our experiments. We can then conclude that as a first approximation the Eu(III) sorption efficiency is heterogeneously distributed over the surface, but the dominant species is the same inner sphere complex throughout.

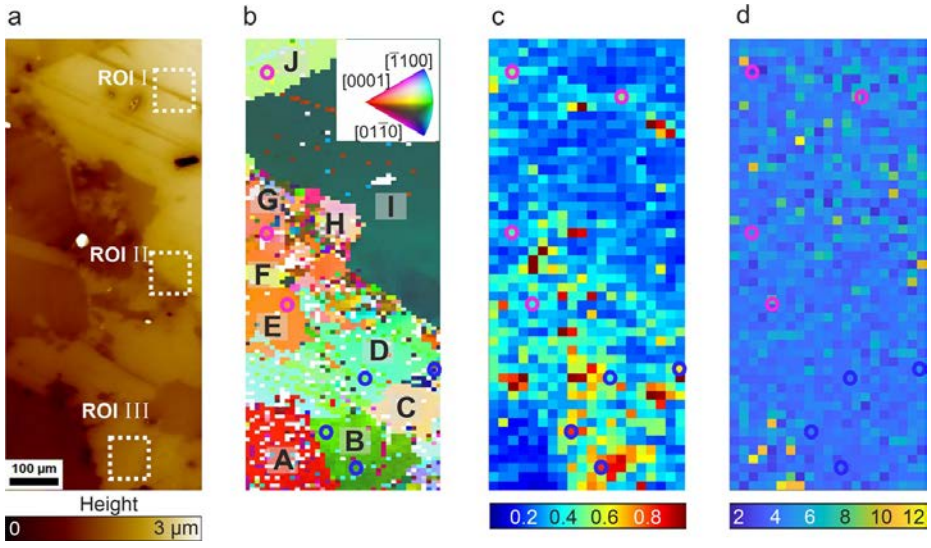

Figure 3. Correlative microscopy of (**a)** Surface height map, field-of-view (FOV) size = 1 mm × 0.4 mm; ROIs I-III refer to three representative sub-regions for model validation (see Figure 6). (**b)** Crystal orientation map based on EBSD data, different colors represent specific crystal orientations, see the legend in Figure S1 for details. **c**, Normalized sorption efficiency (normalized F_1 + F_2 µTRLFS peak sum) with lifetime data points marked with a hollow dot in blue (high

intensity) and purple (low intensity), spatial resolution: 20 µm × 20 µm. **d**, Peak ratio F_2/F_1, indicating speciation/bonding strength, spatial resolution: 20 µm × 20 µm.

Surface nanoroughness parametrization replaces the SSA parametrization towards improved surface complexation modeling. The two datasets of the cleaved and polished surface illustrate the influence of the surface nanotopography is as a major factor for the measured Eu(III) sorption variability (Fig. 2). At the nanometer scale, the spatial configuration surface building blocks defines the surface reactivity and, thus, the sorption efficiency[23]. Nanoroughness can be considered a proxy to quantify the occurrence of such surface building blocks. In order to quantify surface roughness, we select the Sq parameter, the root-mean-square (r.m.s.) deviation of the surface height[41] calculated from the surface topography data, to test its suitability to explain the observed heterogeneous sorption efficiency. Parameter Sq quantifies the height variability more reliably[42] than the arithmetic average roughness Sa. Additionally, we tested the potential use of the surface area ratio parameter, S_{dr}, as a proxy parameter, see Figure S6 in SI.

For the polycrystalline calcite sample, we identify four datasets of different grains, AF, IJHG, EDC, and B by µTRLFS with statistically significantly different Eu(III) sorption (see Table S2 &S3). The crystal orientation within these datasets varies widely with no discernable trend (see Figure S1). No correlation between crystal orientation and Eu(III) sorption efficiency has been found. Furthermore, no correlation between the sorption efficiency and the absolute sample height exists as regions of distinctly different absolute surface heights show similarly low sorption efficiencies (see Figure 3a and c). Grain-specific data (grains: A, B, D, and I) of the sorption efficiency of Eu(III) versus the average Sq roughness of the grain surfaces show a linear correlation ($R^2 = 0.94$), cf. Figure. 4, proving the Sq parameter as a suitable proxy for surface reactivity. Note that effects of crystal orientation may result in a variability of surface nanoroughness, encompassed in the roughness parameter.

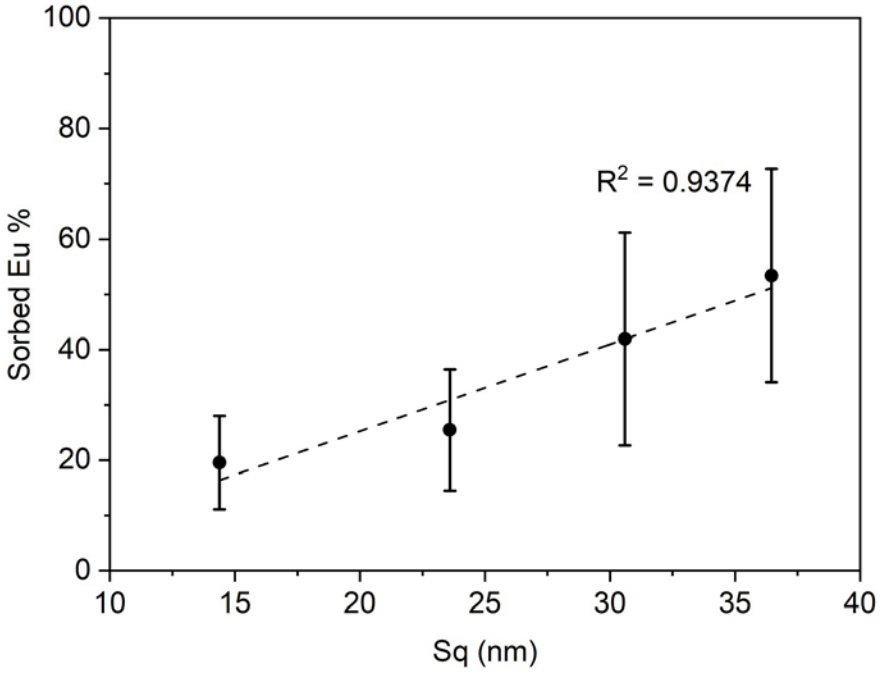

Figure. 4. Normalized amount of europium sorption efficiency based on µTRLFS data collected on grains A, I, D, and B as a function of the Sq roughness of the grain surface.

For a more detailed site-specific investigation as well as for testing the potential use of topographical features for parametrization of the numerical approach, the sorption efficiencies of all pixels of the four different grains with statistically significant different Eu(III) sorption efficiencies were correlated with the Sq value of the field-of-view of each pixel (Figure 5a). Each pixel covers an area of 20 µm × 20 µm (in accordance with the Eu sorption data resolution), which is equivalent to 200 × 200 pixels of the surface topography data shown in Figure 3a. Based on these 115 data points (Figure 5a), only a weak correlation (R^2 = 0.16) between Eu sorption efficiency and Sq value can be identified. Overall, the data seems to be distributed between two regimes, i.e., one regime shows a larger increase of Eu sorption with elevated Sq values up to 40 nm (red color area in Figure 5a), the other regime shows a strong effect of Sq on Eu sorption, mostly covering low includes elevated Sq values up to 80 nm with minor or no correlation with Eu sorption

efficiency (blue color area in Figure 5a). A closer look at the VSI images reveals that in the latter case, the Sq values are strongly influenced by larger surface structures, such as scratches or holes. These features have a large impact on the Sq value but do not appear to significantly impact Eu(III) sorption. Thus, to deconvolve the two regimes (large structures vs. nanoscale roughness) we gradually reduced the field of view for the Sq value calculation down to a minimum of 2.5 × 2.5 μm^2 using consecutive bisection to divide each pixel into a maximum of 64 subpixels, resulting in 64 Sq values for each original pixel. Averaging these sub-pixel Sq values for each original pixel results in a new Sq value for each pixel at a 2.5 × 2.5 μm^2 FOV, and the impact of the larger structures is reduced due to the averaging procedure. The mitigation of the influence of the larger structures is warranted by a more detailed analysis of the correlation between sorption efficiency and Sq values. A separate analysis of subpixels in the ranges of < 5 nm, 5-10 nm, 10-50 nm, and > 50 nm was performed. These ranges were chosen characterize different surface building blocks: The range of 0-10 nm reflects the critical nanoroughness of the surface, the intermediate range is typical for smaller holes left by the EBSD process and dissolution etch pits (10-50 nm), and the range > 50 nm corresponds to large scratches and holes due to the sample preparation. A correlation of the chosen Sq ranges with the sorption efficiency shows correlations only for the first three ranges, i.e., 0 - 50 nm. No correlation was found for Sq values above 50 nm, justifying the de-emphasization of larger structures by the averaging procedure in the previously described (see Figure S2). Mechanistically, this indicates that specific nm-sized surface building blocks such as steps and kinks are the main drivers of the increased sorption efficiency.

Using the newly calculated Sq values for each pixel, we see an increase of the coefficient of determination (R^2) (see SI Figure S5), resulting in a linear correlation at a FOV of 2.5 × 2.5 μm^2 with R^2 = 0.34 (Figure 5b) corresponding to a Pearson's correlation coefficient r of 0.58. While this may appear low, we like to point out that an r of 0.58 is considered to reflect a rather strong

effect for datasets with a large influence of other randomly distributed influences[43]. The motivation of our investigations is to test the predictive power of Sq as a proxy parameter in a polycrystalline system that inherently reflects a combination of several variables. The important prediction of the safety of a nuclear waste repository needs model parameter validation in a realistic system to avoid oversimplification. The data showing a visible spread, nevertheless, the point cloud envelopes a cone of possible linear relationships between Sq and Eu sorption efficiency. This general correlation is potentially and locally affected by several other factors that cause a decreased coefficient of determination for the overall pixel-by-pixel correlation when compared to the averaged grainwise correlation. Influencing factors may include the crystal orientation, the contribution of intrinsic Eu to the µTRLFS signal, the still present impact of larger structures on the Sq value, and effects of unspecific Eu(III) precipitation and calcite dissolution during the sorption experiment. This leads to slightly different valid slopes in different areas of the sample. Furthermore, assuming slightly increased Eu sorption signals due to the presence of incorporated natural Eu and slightly exaggerated Sq values due to large topographic features for the outliers would shift the highest Eu sorption data and highest Sq values to lower values. This would result in a tendency of narrowing the spread of the cone of possible linear relationships (see Figure S7 for illustration). Possible corrections and improvements will be the subject of future investigations. For this study, we choose the linear regression of all data points as the most parsimonious solution to establish a correlation between sorption efficiency and surface nanoroughness. However, while these results provide a quantitative link between surface nanoroughness and sorption efficiency, they cannot be implemented into standard SCM approaches directly. Instead, these models rely on the specific surface area (SSA) and site density (SSD) to quantify the available surface sorption sites interacting with aqueous species at the solid/liquid surface. Typically, SCMs include a description of the electric double layer (e.g. the Gouy-Chapman model[44]) and conventional mass

349 action laws for intrinsic chemical reactions at the surface,[45] but adsorption is ultimately treated as
350 an interaction of metal ions with functional groups uniformly distributed on the surface.
351 Consequently, heterogeneous sorption variabilities as observed in our experiment and previously
352 reported in our previous work[19, 20] cannot be modeled by this standard approach. These variabilities
353 are based on heterogeneously distributed affinities of cations for distinct positions on the calcite
354 surface[46], which are interpreted to be related to the variable amount of coordinated water molecules
355 and Ca-O bond lengths[47] on the different positions of the crystal surface. These underlying affinity
356 variations hold true beyond our specific system, for example, an investigation of the interaction
357 between CO and a Cu surface demonstrated the CO-Cu binding energies at surface defects like
358 steps or kinks to be systematically larger than at the terraces[48]. In general, cations preferably form
359 surface complexes with the typically undercoordinated functional groups at the position of surface
360 defects[49].
361 In surface complexation modeling, the SSD reflects the total surface sites per unit surface area
362 (nm^2), and the SSA reflects the total surface area per unit mass of mineral, which is typically
363 measured using the BET method[50]. The BET-measured surface area shows a dependence on the
364 surface topography of the solid surface, which is linearly correlated with a surface roughness factor
365 , i.e., the ratio of the measured (rough) surface area to the projected (smooth) area[51]. In order to
366 implement spatial variability of the total number of surface sites based on variations of SSD and/or
367 SSA owing to surface roughness variability into an SCM, one could either modify the SSA and fix
368 SSD or vice-versa or modify both at the same time. We choose to vary the SSA and keep the SSD
369 constant, supported by a strong linear correlation of the interpolated surface area and the Sq value
370 (see Figure S8 in SI). As we have established a correlation between surface nanoroughness Sq and
371 sorption efficiency, linking the Sq of our sample to its SSA should enable us to implement the
372 observed interfacial heterogeneity into a predictive model. An SCM was set up (see SI for details)

to establish a quantitative relationship between the Eu sorption efficiency and SSA (Figure 5c). Ultimately, we aim to link our experimental data to literature data using surface data collected by, e.g., BET adsorption techniques. Thus, the concept utilizes a modification of the SSA parameter based on the bulk literature data as a starting point. An opposite choice of varying SSD and keeping SSA constant would yield identical results (see Figure S9) as the process is mathematically equivalent. This allows us to quantitatively link SSA and Sq pixel by pixel (Figure 5d) by cross-referencing the experimental sorption efficiency data (Figure 5b) and the model result (Figure 5c). The quantitative trends in Figs. 5b and d exhibit consistent trends with the investigations of both KMC[38] and MD[5] approaches, which confirms the validity of using surface nanoroughness data as a proxy for the intrinsic crystal surface energy, which has a significant impact on sorption efficiency. Therefore, we utilize this linear trend between SSA and Sq to parameterize a predictive SCM with the assumption that the SSA has a monotonically increasing linear relationship with Sq values.

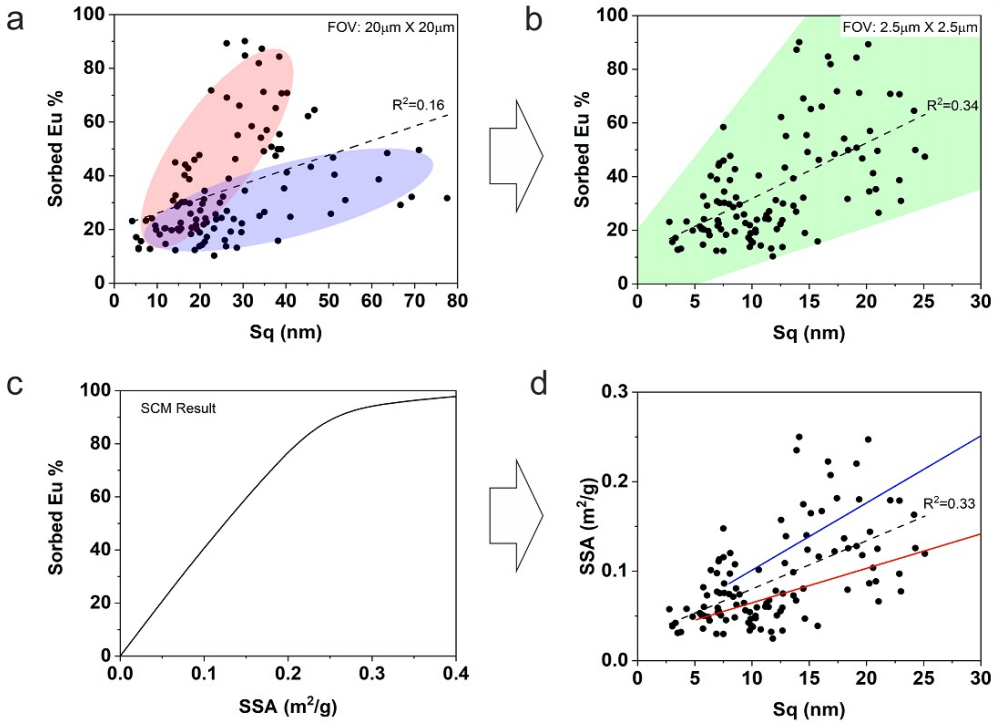

Figure 5. Quantitative correlation between SSA (model) and Sq (experiment) based on experimental data analysis and SCM results. **a**, The scatter plots of measured sorption efficiency versus Sq at a 20 × 20 μm^2 FOV. **b**, The scatter plots of measured sorption efficiency versus Sq at 2.5 × 2.5 μm^2 FOV (right). **c**, SCM results of sorption efficiency versus SSA based on the reactions and thermodynamic data in Table S4. **d**, A scatter plot of SSA versus the averaged Sq at a 2.5 × 2.5 μm^2 FOV. The SSA of each point is calculated by the sorption efficiency through the quantitative curve in Figure 2c. The correlation between SSA and Sq shows a linear curve (gray dashed line) with a coefficient of determination, $R^2 = 0.33$. The red solid line and blue solid line represent the calibration curves used to parameterize the SCM for model validation in ROI I, II, and III, respectively. See text for detailed discussion.

Improved SCM parametrization and model validation. The quantitative relationship between Sq and SSA derived in the previous section is now used to parameterize a spatially resolved SCM using experimentally determined nanoroughness data. Based on the quantitative analysis in Figure 2, we derive the slope of the linear function of SSA vs. Sq as α, with α = 0.0054. The ROIs I, II, and III in Figure 1a are selected as representative regions with available VSI-measured surface topography and sorption data from μTRLFS for model validation. Based on the surface topography of the ROIs (Figure 6a), the corresponding surface roughness maps (Figure 6b) were calculated with a pixel resolution of 10 μm × 10 μm by averaging the Sq value of 2.5 μm × 2.5 μm sub-pixels. We then use the quantitative relationship between Sq and SSA as reflected in α to calculate the SSA of each 10 μm × 10 μm pixel in the three ROIs and, from that, the Eu sorption (Figure 6c). Naturally, the SCM results of the SSA parameterization are very sensitive to the value of α and the spread of the cone of possible linear relationships is wide. Consequently, we performed a sensitivity analysis to optimize the value of α for every ROI. Optimized α values were obtained for the individual ROIs by maximizing the fit of the modeled Eu sorption in each ROI with the

corresponding experimental values (Figure S10). This yielded different calibration curves for each ROI which are plotted in Figure 5d and fall well within the spread of the experimental data, with ROI III exhibiting a steeper slope (blue line with $\alpha = 0.0075$) than the other two (red line with $\alpha = 0.0038$). The SSA modification via Sq parametrization allows us to model similar sorption trends in all three cases. In general, a quantitative comparison of model results (Figure 6c) with the measured data (Figure 6d) shows good agreement within a 20% discrepancy between model and experiment (Figure 6e). In particular, the model underestimates the highest Eu sorption values in ROI III, which may be caused by Eu impurities of the natural calcite crystals, as indicated by the fluorescence lifetime measurement at this point of the sample (see SI Table S5, point 12/48). In contrast to typical SCM approaches that employ a simple uniform SSA value[9, 10], this modified SSA based on Sq analysis allows for the investigation of spatially resolved retention variability based on the variability of crystal surface energy[17]. Choosing the right α will be critical in the feasibility of this approach for predictive modeling and more research needs to be devoted towards the clarification of the varying influences on the relationship between surface topography and surface energy variation.

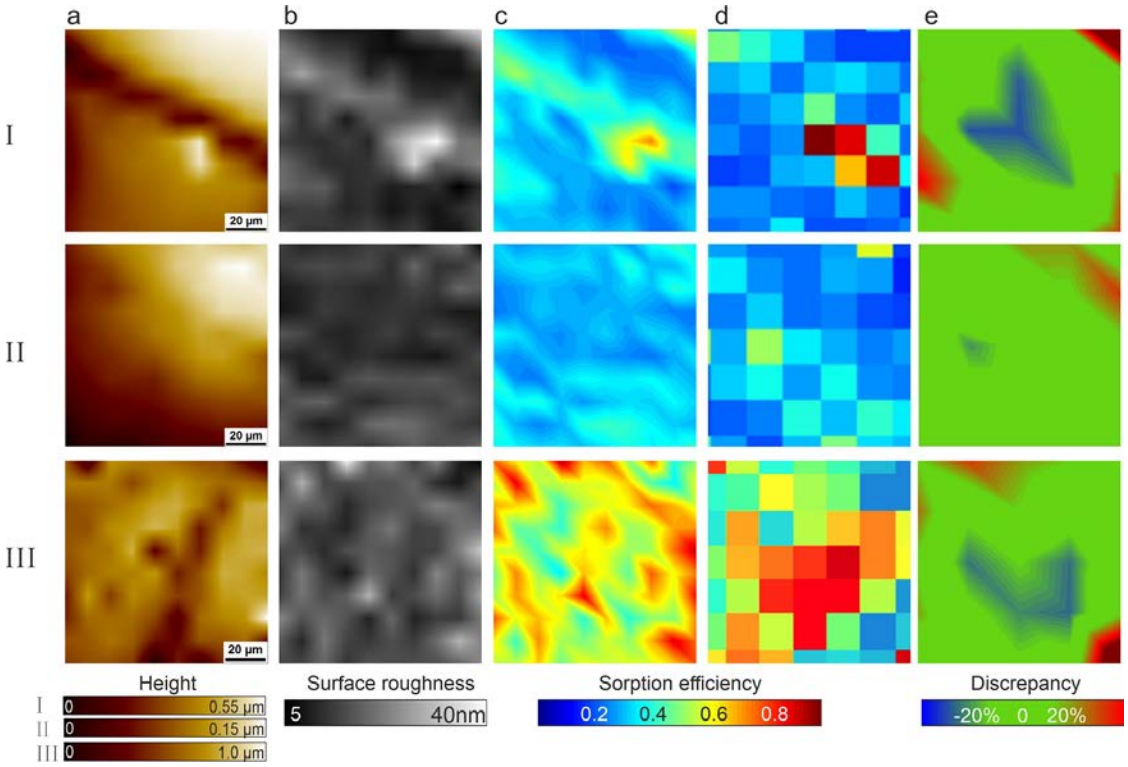

Figure 6. SCM validations in ROIs I, II, and III. **a,** surface topography, spatial resolution = 10 µm × 10 µm; **b,** averaged surface roughness (Sq) at a 2.5 µm × 2.5 µm FOV, spatial resolution = 10 µm × 10 µm; **c**, SCM results of sorption efficiency, spatial resolution = 10 µm × 10 µm; **d**, normalized experimental results of sorption efficiency measured using µTRLFS techniques, spatial resolution = 20 µm × 20 µm; **e,** the ratio of model vs. experimental sorption efficiency. Green color represents a range of +/- 20 % discrepancy, red color: overestimation, blue color: underestimation.

Predicting radionuclide sorption evolution. As a next step, we explore the potential of our improved parameterization approach to predict heterogeneous sorption on the crystal surface of an independent set of experimental data. Figure 7 shows two surface topography maps, measured using phase shifting interferometry (PSI) of a calcite single crystal after 120 minutes (a I) and 135 minutes (a II) of etching, respectively, representing the crystal surface evolution during dissolution. From the topographical data (Figure 7a), we again derived the Sq values, here with a spatial resolution of 0.46 µm × 0.46 µm (Figure 7b), use Sq to derive the SSA with the previously

determined value for α, adapted for the higher resolution (see Figure S4), and predict heterogeneous Eu(III) sorption (Figure 7c) based on our novel SCM parameterization approach.

A first important finding from this prediction is that Eu(III) is preferably adsorbed at surface steps which exhibit higher nanoroughness and kink site densities. In contrast, flat terraces and nearly flat bottoms of the surface pits are predicted to show lower adsorption. For the widening of etch pits on the surface, such as in cross-section A-B in Figure 7, the areas of high surface roughness move outwards with the evolution of the etched pit, resulting in a redistribution of the preferred sorption areas. Another finding with important implications for the evolution of the overall surface efficiency is that the sorption efficiency varies with the evolution of surface topography beyond just a spatial redistribution of the preferred sorption sites. As an example, ROI C shows an overall increase of the Sq value due to the etching which goes along with a 160% increase in sorption efficiency. This enhanced sorption efficiency as a result of the evolving surface structure may be linked to an increase in surface steps and kinks[17] by etching. In contrast to the enhanced sorption efficiency in ROI C, the sorption efficiency of ROI D exhibits a 25% reduction, linked to a reduced Sq due to the removal of surface features by etching. Such behavior is explained by locally contrasting surface step arrangement on a reacting crystal surface. One situation is a constant number and density of single height steps on the crystal surface. The other situation is the formation of step bands due to surface step bunching, resulting in a locally enhanced step density[52].

The overall sorption efficiency of the entire domain and its evolution over time depends on the balance between such subareas. Thus, SSA parameterization via surface nanoroughness in SCM analysis may provide a tool to predict the evolution of radionuclide sorption caused by the changes in surface building blocks. Consequently, the detailed quantitative insight into retention variability gained by this approach may provide a more accurate description of sorption at the pore scale contributing to an enhanced predictive capability on the core scale and beyond. An experimental

validation of such high-resolution modeling is not yet possible using current analytical approaches with limited spatial resolution. Nevertheless, the mechanistic background of specific crystal surface portions showing enhanced kink site densities (Figure 1) and, thus, elevated sorption uptake (Figure 2) provides an opportunity for the validation of such modeling approaches. Consequently, the numerical results predict potential pattern evolution of reacting surfaces and offer opportunities for applications.

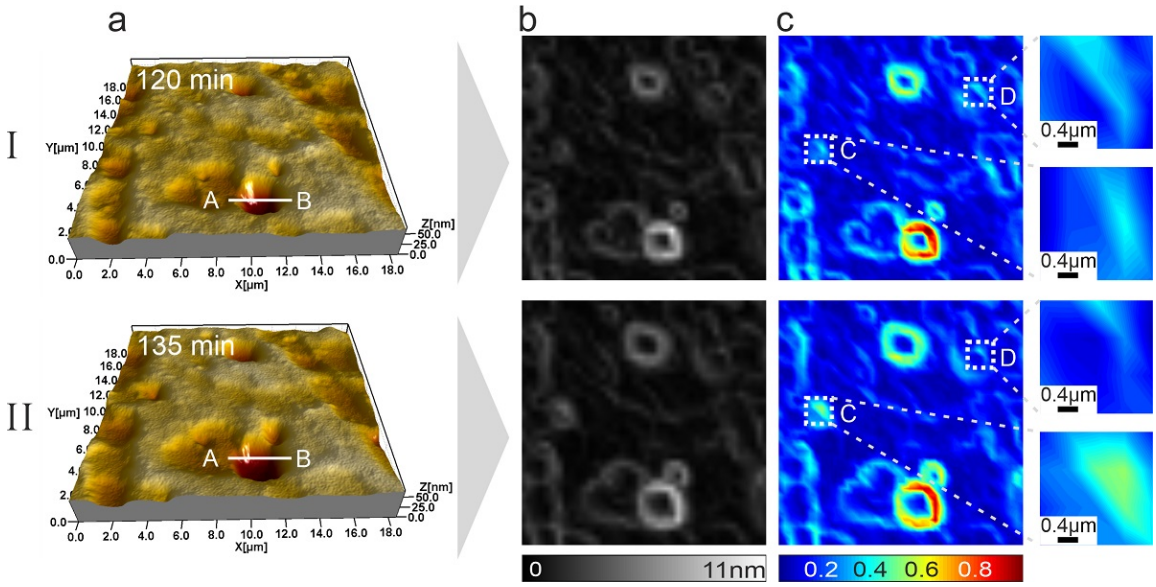

Figure 7. Prediction of the evolution of sorption efficiency for two high spatial resolution data, based on PSI techniques reflecting evolving surfaces at 120 min and 135 min dissolution reaction time. Surface area = 18.5 µm × 18.5 µm. **a**, surface topography, spatial resolution = 0.046 µm × 0.046 µm. **b**, surface roughness (Sq), spatial resolution = 0.46 µm × 0.46 µm. **c**, SCM results of sorption efficiency, spatial resolution = 0.46 µm × 0.46 µm. ROI A-B shows the sorption preference at surface steps rather than the flat terrace. ROIs C and D show the enhanced and reduced sorption efficiency due to the changes in surface topography by etching, respectively.

ACKNOWLEDGMENTS

We gratefully acknowledge funding by the German Federal Ministry of Education and Research (BMBF), grant 02NUK053B and the Helmholtz Association, grant SO-093 (iCross), as well as grant PIE-0007 (CROSSING)

References

1. Stumpf, T.; Bauer, A.; Coppin, F.; Fanghanel, T.; Kim, J. I., Inner-sphere, outer-sphere and ternary surface complexes: a TRLFS study of the sorption process of Eu(III) onto smectite and kaolinite. *Radiochim. Acta* **2002,** *90*, 345-349.
2. Collins, R. N.; Saito, T.; Aoyagi, N.; Payne, T. E.; Kimura, T.; Waite, T. D., Applications of time-resolved laser fluorescence spectroscopy to the environmental biogeochemistry of actinides. *J. Environ. Qual.* **2011,** *40* (3), 731-41.
3. Mandaliev, P.; Stumpf, T.; Tits, J.; Dähn, R.; Walther, C.; Wieland, E., Uptake of Eu(III) by 11Å tobermorite and xonotlite: A TRLFS and EXAFS study. *Geochim. Cosmochim. Acta* **2011,** *75* (8), 2017-2029.
4. Pan, D.; Fan, F.; Wang, Y.; Li, P.; Hu, P.; Fan, Q.; Wu, W., Retention of Eu(III) in muscovite environment: Batch and spectroscopic studies. *Chem. Eng. J.* **2017,** *330*, 559-565.
5. Wolthers, M.; Di Tommaso, D.; Du, Z.; de Leeuw, N. H., Calcite surface structure and reactivity: molecular dynamics simulations and macroscopic surface modelling of the calcite-water interface. *Phys. Chem. Chem. Phys.* **2012,** *14* (43), 15145-57.
6. Churakov, S. V.; Liu, X., Quantum-chemical modelling of clay mineral surfaces and clay mineral–surface–adsorbate interactions. In *Surface and Interface Chemistry of Clay Minerals*, 2018; pp 49-87.
7. Parkhurst, D. L.; Appelo, C. A. J. *Description of input and examples for PHREEQC version 3: a computer program for speciation, batch-reaction, one-dimensional transport, and inverse geochemical calculation*; 6-A43; Reston, VA, USA, 2013.
8. Barnett, M. O.; Jardine, P. M.; Brooks, S. C., U(VI) Adsorption to Heterogeneous Subsurface Media: Application of a Surface Complexation Model. *Environ. Sci. Technol.* **2002,** *2002* (36), 937-942.
9. Dong, W.; Tokunaga, T. K.; Davis, J. A.; Wan, J., Uranium(VI) adsorption and surface complexation modeling onto background sediments from the F-Area Savannah River Site. *Environ. Sci. Technol.* **2012,** *46* (3), 1565-71.
10. Dong, W.; Wan, J., Additive surface complexation modeling of uranium(VI) adsorption onto quartz-sand dominated sediments. *Environ. Sci. Technol.* **2014,** *48* (12), 6569-77.
11. Van Cappellen, P.; Charlet, L.; Stumm, W.; Wersin, P., A surface complexation model of the carbonate mineral-aqueous solution interface. *Geochim. Cosmochim. Acta* **1993,** *57*, 3505-3518.
12. Waite, T. D.; Davis, J. A.; Payne, T. E.; Waychunas, G. A.; Xu, N., Uranium(VI) adsorption to ferrihydrite: Application of a surface complexation model. *Geochim. Cosmochim. Acta* **1994,** *58* (24), 5465-5478.
13. Pokrovsky, O. S.; Schott, J., Surface Chemistry and Dissolution Kinetics of Divalent Metal Carbonates. *Environ. Sci. Technol.* **2002,** *36*, 426-432.
14. Vanson, J. M.; Coudert, F. X.; Klotz, M.; Boutin, A., Kinetic Accessibility of Porous Material Adsorption Sites Studied through the Lattice Boltzmann Method. *Langmuir* **2017,** *33* (6), 1405-1411.

15. Steefel, C. I.; Carroll, S.; Zhao, P.; Roberts, S., Cesium migration in Hanford sediment: a multisite cation exchange model based on laboratory transport experiments. *J. Contam. Hydrol.* **2003,** *67* (1-4), 219-246.
16. Wersin, P.; Soler, J. M.; Van Loon, L.; Eikenberg, J.; Baeyens, B.; Grolimund, D.; Gimmi, T.; Dewonck, S., Diffusion of HTO, Br^-, I^-, Cs^+, $^{85}Sr^{2+}$ and $^{60}Co^{2+}$ in a clay formation: Results and modelling from an in situ experiment in Opalinus Clay. *Appl. Geochem.* **2008,** *23* (4), 678-691.
17. Fischer, C.; Kurganskaya, I.; Schäfer, T.; Lüttge, A., Variability of crystal surface reactivity: What do we know? (Review Article). *Appl. Geochem.* **2014,** *43*, 132-157.
18. White, A. F.; Brantley, S. L., The effect of time on the weathering of silicate minerals: why do weathering rates differ in the laboratory and field? *Chem. Geol.* **2003,** *202* (3-4), 479-506.
19. Molodtsov, K.; Schymura, S.; Rothe, J.; Dardenne, K.; Schmidt, M., Sorption of Eu(III) on Eibenstock granite studied by microTRLFS: A novel spatially-resolved luminescence-spectroscopic technique. *Sci. Rep.* **2019,** *9* (1), 6287.
20. Molodtsov, K.; Demnitz, M.; Schymura, S.; Jankovsky, F.; Zuna, M.; Havlova, V.; Schmidt, M., Molecular-Level Speciation of Eu(III) Adsorbed on a Migmatized Gneiss As Determined Using µTRLFS. *Environ. Sci. Technol.* **2021**.
21. Noiriel, C.; Daval, D., Pore-Scale Geochemical Reactivity Associated with CO2 Storage: New Frontiers at the Fluid-Solid Interface. *Acc. Chem. Res.* **2017,** *50* (4), 759-768.
22. Bollermann, T.; Fischer, C., Temporal evolution of dissolution kinetics of polycrystalline calcite. *Am. J. Sci.* **2020,** *320* (1), 53-71.
23. Mehmood, F.; Kara, A.; Rahman, T. S.; Henry, C. R., Comparative study of CO adsorption on flat, stepped, and kinked Au surfaces using density functional theory. *Phys. Rev. B* **2009,** *79* (7).
24. Binnemans, K., Interpretation of europium(III) spectra. *Coord. Chem. Rev.* **2015,** *295*, 1-45.
25. Schmidt, M.; Stumpf, T.; Marques Fernandes, M.; Walther, C.; Fanghanel, T., Charge compensation in solid solutions. *Angew. Chem. Int. Ed. Engl.* **2008,** *47* (31), 5846-50.
26. Zachara, J. M.; Cowan, C. E.; Resch, C. T., Sorption of divalent metals on calcite. *Geochim. Cosmochim. Acta* **1991,** *55* (6), 1549-1562.
27. Carroll, S. A.; Bruno, J., Mineral-Solution Interactions in the U(VI)-CO_2-H_2O System. *Radiochim. Acta* **1991,** *52*, 187-193.
28. Zavarin, M.; Roberts, S. K.; Hakem, N.; Sawvel, A. M.; Kersting, A. B., Eu(III), Sm(III), Np(III), Pu(III), and Pu(IV) sorption on calcite. *Radiochim. Acta* **2005,** *93*, 93-102.
29. Hellebrandt, S. E.; Hofmann, S.; Jordan, N.; Barkleit, A.; Schmidt, M., Incorporation of Eu(III) into Calcite under Recrystallization conditions. *Sci. Rep.* **2016,** *6*, 33137.
30. Zeisig, A.; Siegesmund, S.; Weiss, T., Thermal expansion and its control on the durability of marbles. *Geological Society, London, Special Publications* **2002,** *205* (1), 65-80.
31. Mahan, J. E., Physical vapor deposition of thin films. *Physical Vapor Deposition of Thin Films, by John E. Mahan, pp. 336. ISBN 0-471-33001-9. Wiley-VCH, January 2000.* **2000**, 336.
32. Halfpenny, A., Some important practical issues for the collection and manipulation of electron backscatter diffraction (EBSD) data from geological samples. *Journal of the Virtual Explorer* **2010,** *35*.
33. Horrocks, W. D.; Sudnick, D. R., Lanthanide ion probes of structure in biology. Laser-induced luminescence decay constants provide a direct measure of the number of metal-coordinated water molecules. *Journal of the American Chemical Society* **1979,** *101* (2), 334-340.

34. Kimura, T.; Choppin, G. R., Luminescence study on determination of the hydration number of Cm(III) *J. Alloys Compd.* **1994,** *213-214*, 313-317.
35. Thoenen, T.; Hummel, W.; Berner, U.; Curti, E. *The PSI/Nagra Chemical Thermodynamic Database 12/07*; Villigen PSI, Switzerland, 2014.
36. Petersen, M. A.; van den Berg, J.-A.; Ciobîcă, I. M.; van Helden, P., Revisiting CO Activation on Co Catalysts: Impact of Step and Kink Sites from DFT. *ACS Catalysis* **2017,** *7* (3), 1984-1992.
37. de Assis, T. A.; Aarão Reis, F. D. A., Dissolution of minerals with rough surfaces. *Geochim. Cosmochim. Acta* **2018,** *228*, 27-41.
38. Kurganskaya, I.; Churakov, S. V., Carbonate Dissolution Mechanisms in the Presence of Electrolytes Revealed by Grand Canonical and Kinetic Monte Carlo Modeling. *J. Phys. Chem. C* **2018,** *122* (51), 29285-29297.
39. Piriou, B.; Fedoroff, M.; Jeanjean, J.; Bercis, L., Characterization of the Sorption of Europium(III) on Calciteby Site-Selective and Time-ResolvedLuminescence Spectroscopy. *J. Colloid Interface Sci.* **1997,** *194*, 440-447.
40. Stipp, S. L. S.; Christensen, J. T.; Lakshtanov, L. Z.; Baker, J. A.; Waight, T. E., Rare Earth element (REE) incorporation in natural calcite: Upper limits for actinide uptake in a secondary phase. *Radiochim. Acta* **2006,** *94*, 523-528.
41. Fischer, C.; Luttge, A., Converged surface roughness parameters A new tool to quantify rock surface morphology and reactivity alteration. *Am. J. Sci.* **2007,** *307* (7), 955-973.
42. Thomas, T. R., *Rough Surfaces*. Imperial College Press: 1999.
43. Cohen, J., A Power Primer. *Psychol. Bull.* **1992,** *112*, 155-159.
44. Grahame, D. C., The Electrical Double Layer and the Theory of Electrocapillarity. *Chem. Rev.* **1947,** *41* (3), 441-501.
45. Sverjensky, D. A., Physical surface-complexation models for sorption at the mineral-water interface. *Letters to Nature* **1993,** *364*, 776-780.
46. Reeder, R. J., Interaction of divalent cobalt, zinc, cadmium, and barium with the calcite surface during layer growth. *Geochim. Cosmochim. Acta* **1996,** *60* (9), 1543-1552.
47. Wolthers, M.; Charlet, L.; Van Cappellen, P., The surface chemistry of divalent metal carbonate minerals; a critical assessment of surface charge and potential data using the charge distribution multi-site ion complexation model. *Am. J. Sci.* **2008,** *308* (8), 905-941.
48. Vollmer, S.; Gregor, W.; Christof, W., Determination of site specific adsorption energies of CO on copper. *Catal. Lett.* **2001,** *77*, 97-101.
49. Lützenkirchen, J., Surface Complexation Models of Adsorption. In *Encyclopedia of Surface and Colloid Science*, Second Edition ed.; Somasundaran, P., Ed. Taylor & Francis: 2011; pp 5899-5914.
50. Lüttge, A.; Arvidson, R. S., The Mineral-Water Interface. In *Kinetics of Water-Rock Interaction*, S., B.; J., K.; A., W., Eds. Springer: New York, NY, 2008; pp 73-107.
51. Beckingham, L. E.; Mitnick, E. H.; Steefel, C. I.; Zhang, S.; Voltolini, M.; Swift, A. M.; Yang, L.; Cole, D. R.; Sheets, J. M.; Ajo-Franklin, J. B.; DePaolo, D. J.; Mito, S.; Xue, Z., Evaluation of mineral reactive surface area estimates for prediction of reactivity of a multi-mineral sediment. *Geochim. Cosmochim. Acta* **2016,** *188*, 310-329.
52. Yagi, K.; Minoda, H.; Degawa, M., Step bunching, step wandering and faceting: self-organization at Si surfaces. *Surf. Sci. Rep.* **2001,** *43* (2-4), 45-126.